JMEPEG
https://doi.org/10.1007/s11665-022-07755-8

1059-9495/$19.00

TECHNICAL ARTICLE

Machining Complex Profile on Nickel-Aluminum-Bronze Alloy through Wire Electric Discharge Machining Process using Zinc-Coated Brass Wire

D.K. Sonkar, S. Saha, S.R. Maity, and S. Dey

Submitted: 8 September 2022 / Revised: 30 October 2022 / Accepted: 2 December 2022

WEDM is efficient in machining complicated profiles with high dimensional accuracy. The Nickel-aluminum-bronze (NAB) is a high-strength alloy with exceptional corrosion-resistant properties and is abundantly used in marine applications such as propellers, valves, and seawater pumps. The previous literature reports numerous instances of WEDM-induced simple profiles on NAB alloy employing brass and molybdenum wires; however, the WEDM of detailed profiles on NAB alloy using brass wire encapsulated with zinc layer is scarce to find. Hence, in the present article, we proposed an experimental framework to create complex profiles on NAB alloy using the zinc-enveloped brass wire in the WEDM process. The control variables, namely the pulse on time, servo voltage, current, and pulse off time, were varied to report their influence on the experimentally determined machining time (MT), kerf width (KW), and corner error (CE). The statistical analysis revealed that pulse on time affects the KW and CE dominantly, whereas the current has high relative significance when MT is concerned. FESEM images showed that WEDM processing at high discharge energy settings generated many large-sized voids, large melted deposits, deep craters, and microcracks on the surface. Conversely, WEDM processing at low discharge energy settings caused small-sized voids, small melted deposits, and shallow craters. Microcracks are not visible on the surface after WEDM processing at a low discharge energy level. Energy dispersive x-ray (EDX) analysis discerned the substantial deposition of zinc on the machined surface from the zinc-coated brass wire ensuing the machining operation.

Keywords corner error, energy dispersive x-ray, field emission scanning electron microscopy, kerf width, machining time, nickel-aluminum-bronze alloy, wire electric discharge machining

1. Introduction

The rising trend in product fabrication using advanced materials has posed severe challenges to the entire manufacturing industry (Ref 1). Nickel-aluminum-bronze (NAB) alloy is an advanced material with high strength, high corrosion resistance, and high biofouling resistance, which is widely used in maritime applications such as ship propellers, pumps, and valves (Ref 2). Since NAB alloy is a copper-based alloy, the high ductility of copper leads to continuous chips, resulting in irregular machined surfaces during conventional machining. Al-Ethari and Hamza (Ref 3) scrutinized the impact of machining conditions on tool wear while drilling NAB alloy. Zhong et al. (Ref 4) proposed a strategy to determine the Johnson–Cook model's constitutive parameters in NAB alloy machining. They analyzed the influence of process conditions on the cutting force of this alloy. Zhou et al. (Ref 5) proposed an analytical model to estimate the residual stress under the mechanical and thermal loading during the end milling of NAB alloy. Having acquainted with the difficulties faced during conventional machining of NAB alloy, researchers are intrigued to carry out the machining of Cu-based alloys employing unconventional machining approaches. Of all the unconventional machining approaches, WEDM is preferable because it can generate complicated shapes with high dimensional accuracy (Ref 6-8).

The material erosion in the WEDM process commences when the electric spark is generated amid the running wire electrode and the workpiece material. This electric spark induces extensive thermal energy, i.e., a temperature of around 10,000 °C to melt and vaporize the work material. The melted debris from the work material are then cleaned by the dielectric fluid injected from the top and bottom nozzles, resulting in craters on the machined surface. The simplified view of the WEDM process is illustrated in Fig. 1. Since WEDM is performed using spark discharges, the instantaneous gap state condition, the discharge type, and the discharge frequency influences the process performances and are dependent on the considered process parametric settings. This inspired the researchers to carry out process parametric optimization and investigate process parameters' influence on process performances. For instance, Majumder and Maity (Ref 9) optimized the process features such as dielectric pressure, discharge current, wire feed, pulse duration, and wire tension for

D.K. Sonkar, S.R. Maity, and **S. Dey**, Department of Mechanical Engineering, National Institute of Technology Silchar, Silchar, Assam, India; and **S. Saha**, Department of Mechanical Engineering, St. Martin's Engineering College, Secunderabad, Telangana, India. Contact e-mail: saikat.jumtech@gmail.com.

Published online: 19 December 2022

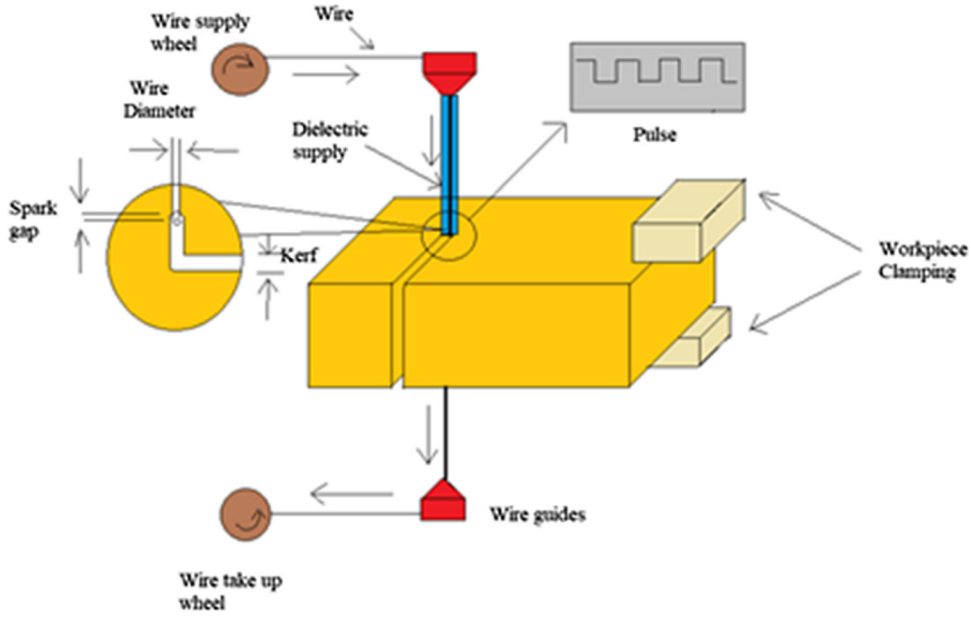

Fig. 1 Simplified representation of WEDM process

microhardness and surface roughness in WEDM of nitinol shape memory alloy. Tonday and Tigga (Ref 10) optimized the WEDM machining parameters, namely the cutting voltage, wire feed, pulse on time, flushing pressure, and pulse off time to acquire the minimum surface roughness, and minimum time for Inconel 718. Kumar et al. (Ref 11) exploited the analytical hierarchy process and genetic algorithm to optimize the process variables for the three response variables, such as the material removal rate, spark gap, and surface roughness in WEDM of aluminum hybrid composites. Sharma et al. (Ref 12) examined the influence of varying wire electrode material on cutting rate and surface integrity aspects in WEDM of Inconel 706 superalloy. It was reported that lower SR, smoother topography, and thin recast layer was achieved with the hard brass wire. Whereas higher cutting speed was achieved with zinc-coated wire. Bisaria and Shandilya (Ref 13) scrutinize the role of spark energy, peak current, and spark frequency on average cutting rate, surface roughness, and surface integrity during the WEDM of Nimonic C-263 superalloy. Han and his group examined the relative domination of different process features' on the surface quality of Cr12 alloy steel ensuing WEDM with brass wire (Ref 14). Likewise, Sadeghi et al. (Ref 15) led an experimental inquiry whereby the role of different machining parameters on process efficiency is emphasized while processing AISI D5/DIN 1.2601 steel through WEDM. In another study, Sharma et al. (Ref 16) reported that the dimensional accuracy and cutting rate are hugely responsive to pulse on time in WEDM of a very strong low-alloy steel. Yu et al. (Ref 17) characterized the influence of input features on cutting speed, the machined groove's width, and surface finish in WEDM of silicon (polycrystalline form) with brass wire, whereas, Patil and Brahmankar (Ref 18) scrutinize the domination of different process features on the kerf width, cutting rate, and surface undulation while WEDM of alumina particle-reinforced aluminum matrix composites (Al/Al_2O_3-p) deploying coated brass wire as the tool electrode. Saha et al. (Ref 19) reported the impact of five process features on the geometrical imprecision of square profile cut in WEDM of A286 superalloy. Likewise, another research group scrutinized the impact of machining features on process efficiency while creating a square profile in WEDM operation (Ref 20, 21). Gupta et al. (Ref 22) investigated the influence of input features on the kerf size while processing a very strong low-alloy steel through WEDM. They concluded that the quality of kerf ameliorates with an increasing trend in the servo voltage and pulse off time. At the same time, the quality of kerf degrades with an increment in pulse on time and peak current. Lakshmanan et al. (Ref 23) portrayed the role of three electrical parameters and a mechanical parameter on the rate of material erosion and the dimension of kerf in WEDM of Nickel-aluminum-bronze alloy exploiting molybdenum wire. The foregoing literature discusses the works on WEDM, which are based on simple geometries. However, in complicated profiles such as sharp corners and curved geometries, the problem of wire lag associated with the WEDM process is a serious issue and affects the geometrical accuracy. As a result, numerous research attempts have been documented over the past few years, which suggested various strategies to reduce the influence of wire lag and improve corner accuracy (Ref 24–27). Modifying process parameters is turned out to be an effective strategy for manipulating the wire lag and the ensuing corner accuracy. In this regard, the research community has examined the influence of various process variables on corner accuracy. Such as, Yan et al. (Ref 28) examined the effect of process variables, i.e., pulse off time, the pulse on time, peak current, and magnetic field power on the corner accuracy of Q235 steel in WEDM. Likewise, Mandal et al. (Ref 29) used WEDM of Al 7075 alloy to examine corner accuracy. They reported that the duration of pulse, the interval between pulses, and servo voltage influence corner accuracy significantly. In another study, Bisaria et al. (Ref 30) probed the role of spark duration, wire tension, spark redundant time, servo voltage, and wire feed rate of wire on corner error while WEDM of $Ni_{50\cdot89}Ti_{49.11}$ shape memory alloy with 60°, 90°, and 120° triangular profiles.

The literature review presented in the preceding paragraphs shows that the WEDM of complicated profiles on NAB alloy is not explored. Besides, the WEDM of NAB alloy is carried out using only brass and molybdenum wires. Therefore, the novelty of the present work is to generate a complicated profile during WEDM on NAB alloy wherein we have assessed the corner error as the response parameter apart from the other two conventional response parameters, i.e., machining time and kerf width. We intend to statistically investigate the influence of four process variables, i.e., pulse on time, pulse off time, current, and servo voltage, on the three salient performance variables such as the machining time (MT), kerf width (KW), and corner error (CE). Parametric analyses have been conducted to reveal the trend of variations of the response parameters with the variation in the process inputs. In addition, while machining, the wire material which was considered is a zinc-coated brass wire which further adds to the novelty of the present work as there is no work reported on WEDM of NAB alloy using zinc-coated brass wire. The post-machining microstructures of the machined surface were revealed using FESEM, and elemental weight percent analysis was revealed with EDX analysis which also manifests the compositional variation undergone by the machined surface of NAB alloy due to the use of zinc-coated brass wire. Thereafter, the paper is divided as follows: Sect. 2 describes the materials and methods adopted in the current study, Sect. 3 elaborates the findings of the present study, Sect. 4 reports the surface topography and elemental transformation analysis and lastly Sect. 5 portrays the conclusions drawn in the paper.

2. Materials and Methods

In the current analysis, the complex profiles of nickel-aluminum-bronze (NAB) alloy are obtained experimentally by using the WEDM process. The constituents of NAB alloy specimens comprises of Al (13 wt.%), Fe (6 wt.%), Ni (4 wt.%), Mn (0.71 wt.%), Zn (0.32 wt.%), Sn (0.166 wt.%), and Cu (75.804 wt.%). The concave-convex profiles (refer to Fig. 2b) are produced on the rectangular specimen plates with 200 × 30 × 15 mm. The WEDM experiments are carried out in Electronica-Tool master 6S wire electrical discharge machine (Table size: 875 × 595 mm, accuracy: 10 microns) wherein, the brass wire (diameter = 0.25 mm) overlaid with zinc was selected as the wire electrode. A detailed representation of the WEDM setup is presented in Fig. 2(a). The input process variables and their corresponding levels were selected based on preliminary experiments and previous works (Ref 31, 32). Apart from the parameters shown in Table 1, the other parameters were maintained at constant values (such as servo feed rate = 120 mm/min, wire feed rate = 4 m/min, water pressure = 15 kg/cm^2, and wire tension = 7 N).

The WEDM experiments were performed for total thirty samples obtained from the face-centered central composite design by enforcing the different levels of considered process features; the responses (machining time, kerf width, and corner error) were recorded for each sample by using the suitable experimental approaches (refer to Table 2 for the sample wise obtained observations). The corner error (see in Fig. 2d) and kerf width (see in Fig. 2e) were measured using an optical microscope (see in Fig. 2c). The magnitude of wire lag was accounted in determining the corner error. The three trial runs of each sample were performed, and the average of responses was used for further analysis. To draw comprehensive insights into the surface characteristics of machined surfaces at the microscopic level (see Fig. 2g), we exploited the field emission scanning electron microscope (FESEM) in conjunction with EDX mapping (see in Fig. 2f).

3. Results and Discussion

3.1 Mathematical Modeling and Statistical Analysis

The response surface methodology (RSM) is the procedure adopted to model the relationship between the process features and responses. A full quadratic model (inclusive of linear, higher-order, and interaction terms) is used to approximate the correlation between the performance measures and process parameters due to the process complexity. The general form of full quadratic model is revealed with the help of Eq 1.

$$\gamma = \alpha_0 + \alpha_1 x_1 + \alpha_2 x_2 + \alpha_3 x_3 + \alpha_4 x_4 + \alpha_{11} x_1^2 + \alpha_{22} x_2^2 + \alpha_{33} x_3^2 + \alpha_{44} x_4^2 + \alpha_{12} x_1 x_2 + \alpha_{13} x_1 x_3 + \alpha_{14} x_1 x_4 + \alpha_{23} x_2 x_3 + \alpha_{24} x_2 x_4 + \alpha_{34} x_3 x_4 \quad \text{(Eq 1)}$$

where γ is the response variable, and x_1, x_2, x_3 and x_4 are the explanatory variables. α_1, α_2, α_3 and α_4 indicate the linear effects of x_1, x_2, x_3 and x_4. α_{11}, α_{22}, α_{33}, and α_{44} indicate the quadratic effects of x_1, x_2, x_3 and x_4 and α_{12}, α_{13}, α_{14}, α_{23}, α_{24}, and α_{34} indicate the linear-by-linear interaction between x_1, x_2, x_3 and x_4. The regression coefficients are estimated with the least-square procedure. The models for the three responses along with their R^2 values are shown below:

$$\mathrm{MT} = 10980 - 22.4A + 0.3B - 1663.1C - 1.34D + 0.021A^2 + 0.016B^2 + 67.31C^2 - 0.0026D^2 + 0.0242\mathrm{A} * \mathrm{B} + 1.226\mathrm{A} * \mathrm{C} + 0.0370\mathrm{A} * \mathrm{D} - 0.475\mathrm{B} * \mathrm{C} + 0.0256\mathrm{B} * \mathrm{D} - 0.341\mathrm{C} * \mathrm{D} \quad \text{(Eq 2)}$$

(R^2 = 0.9974, Adjusted R^2 = 0.9950, Predicted R^2 = 0.9813)

$$\mathrm{KW} = 4.58 - 0.085A - 0.0343B + 0.186C + 0.0069D + 0.0004441A^2 + 0.000221B^2 + 0.00203C^2 - 0.000035D^2 + 0.000105\mathrm{A} * \mathrm{B} - 0.001700\mathrm{A} * \mathrm{C} - 0.000013\mathrm{A} * \mathrm{D} + 0.000200\mathrm{B} * \mathrm{C} - 0.000083\mathrm{B} * \mathrm{D} - 0.000050\mathrm{C} * \mathrm{D} \quad \text{(Eq 3)}$$

(R^2 = 0.9660, Adjusted R^2 = 0.9342, Predicted R^2 = 0.8290)

$$\mathrm{CE} = 1862 - 30.8A + 8.96B - 43.2C + 1.52D + 0.1308A^2 - 0.0666B^2 + 0.71C^2 - 0.0108D^2 - 0.0269\mathrm{A} * \mathrm{B} + 0.242\mathrm{A} * \mathrm{C} - 0.0042\mathrm{A} * \mathrm{D} + 0.058\mathrm{B} * \mathrm{C} - 0.0216\mathrm{B} * \mathrm{D} + 0.0540\mathrm{C} * \mathrm{D} \quad \text{(Eq 4)}$$

(R^2 = 0.9804, Adjusted R^2 = 0.9620, Predicted R^2 = 0.8585).

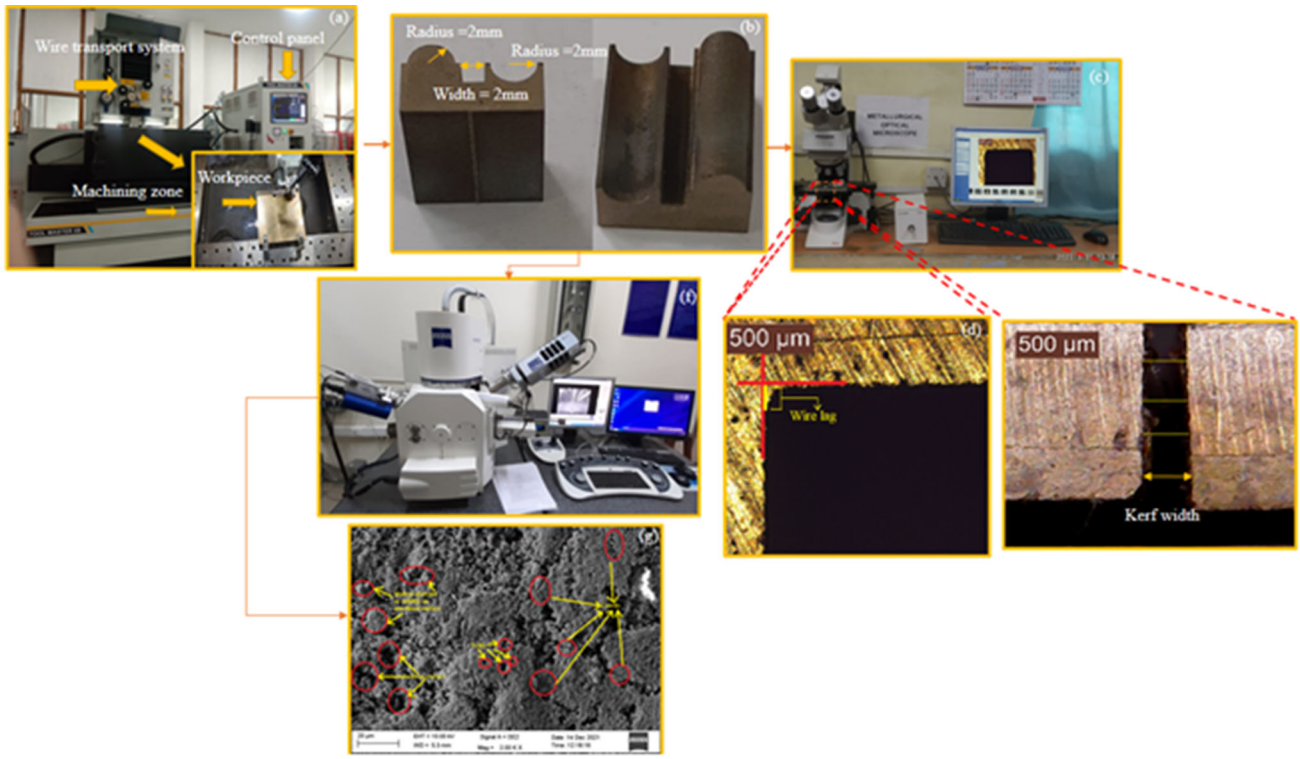

Fig. 2 (a) WEDM machine tool setup, (b) complex profile with dimension, (c) optical microscope, (d) corner error, (e) kerf width, (f) FESEM setup, and (g) machined surface at microscopic level

Table 1 Input process features with their units and levels

Parameters	Level 1	Level 2	Level 3
Pulse on time, μs	118	123	128
Pulse off time, μs	40	45	50
Current, Ampere	10	11	12
Servo voltage, Volt	30	40	50

The variance analysis of individual models for MT, KW, and CE is presented in Table 3, wherein the *p*-values exhibited by all the models are observed to be lower than 0.05, implying that models are statistically significant.

The Pareto analysis conducted for the machining time illustrated in Fig. 3(a) reveals that current (*C*) is the relatively most significant process variable, followed by the square term of the current (CC), pulse on time (*A*), the interaction between current and pulse on time (AC), and servo voltage (*D*). The significance of pulse off time (*B*) is observed to be relatively lower when compared with the other variables. On the other hand, the Pareto analysis for kerf width (refer to Fig. 3b) exhibited the high relative significance of pulse on time (*A*) followed by current (*C*), servo voltage (*D*), and pulse off time (*B*). The interaction between pulse on time (*A*) and current (*C*) is also observed to be statistically significant for the kerf width. The Pareto chart analysis for corner error (refer to Fig. 3c) revealed that similar to the statistical model of the kerf width, all the process variables are found to be statistically significant in the order of pulse on time (*A*), current (*C*), pulse off time (*B*), and servo voltage (*D*). The square term of the pulse on time (AA) is also found statistically significant for the corner error.

3.2 Parametric Influence on WEDM Performance Measures

In this section, we intend to investigate the role of process parameters on WEDM performance measures (MT, KW, and CE) with the help of perturbation plots and 3-D response surfaces. The perturbation plot assists in demonstrating the relative influence of parameters on responses at a certain location in the design space. A perturbation plot corresponding to the machining time (MT) is shown in Fig. 4(a) to highlight the relative influence of control parameters. The peak current (*C*) has a massive effect on machining time, evidenced by its steep slope. The rest of the parameters have relatively less steep slopes, with pulse off time (*B*) and servo voltage (*D*) being the two with the lowest steep slopes, indicating the relatively least significance of these parameters on machining time. The perturbation plot in Fig. 4(b) depicts the relative influence of process parameters on kerf width (KW). It can be inferred that the kerf width is more sensitive to pulse on time (*A*) and peak current (*C*) as the curves corresponding to these parameters are relatively steeper. In contrast, the kerf width is relatively less sensitive to pulse off time (*B*) and servo voltage (*D*) which is evident from the less steep slopes of the curves corresponding to these parameters. Figure 4(c) shows the perturbation plot for corner error (CE). The plot shows that the pulse on time and peak current significantly influences the corner error as the slope of the curves corresponding to these parameters are relatively steeper. On the other hand, the pulse off time and servo voltage have the most negligible influence on corner error as the slope of the curves corresponding to these parameters is relatively less steep. It is noteworthy to mention that the observations gathered from the perturbation plots is found in agreement with the Pareto analysis presented in Fig. 3. With this information, we extend our discussion further to demon-

Table 2 Experimental settings with corresponding responses

Sl. No.	Pulse on time, μs	Pulse off time, μs	Current, Ampere	Servo voltage, Volt	Machining time, min	Kerf width, mm	Corner error, μm
1	123	40	11	40	16.15	0.385	152.21
2	123	45	11	40	17.24	0.379	148.896
3	118	50	10	50	172.11	0.262	125.168
4	123	45	11	40	17.28	0.371	148.196
5	118	40	12	50	20.35	0.382	147.71
6	128	40	12	50	17.34	0.447	171.692
7	128	40	12	30	16.26	0.478	178.417
8	128	50	12	50	18.54	0.415	167.23
9	123	45	11	40	17.24	0.376	148.53
10	123	45	11	50	17	0.328	144.686
11	118	50	12	30	17.31	0.388	145.22
12	118	45	11	40	18.3	0.313	141.2
13	118	50	12	50	21.13	0.352	136.02
14	123	45	10	40	151.13	0.339	144.69
15	118	50	10	30	165.09	0.305	132.342
16	118	40	10	50	162.31	0.317	130.345
17	123	45	11	30	15.31	0.394	152.93
18	123	45	11	40	16.54	0.374	148.986
19	128	40	10	50	139.32	0.404	158.18
20	123	45	12	40	16.32	0.394	156.49
21	128	45	11	40	15.57	0.438	165.11
22	128	50	10	50	162.5	0.387	149.4
23	128	50	10	30	127.17	0.417	154.837
24	123	45	11	40	17.15	0.372	148.21
25	128	50	12	30	19.27	0.454	170.82
26	123	50	11	40	17.5	0.355	144.23
27	118	40	10	30	156.5	0.335	136.15
28	123	45	11	40	17.32	0.374	147.912
29	128	40	10	30	125	0.424	160.85
30	118	40	12	30	16.59	0.395	140.63

Table 3 Variance analysis for MT, KW, and CE

Response variable	Source	Sum of squares	df	Mean square	F-value	*p*-value	
MT	Model	1.149E + 05	14	8206.05	419.18	0.0001	Significant
	Residual	293.65	15	19.58			
	Total	1.152E + 05	29				
KW	Model	0.0626	14	0.0045	30.40	0.0001	Significant
	Residual	0.0022	15	0.0001			
	Total	0.0648	29				
CE	Model	4412.39	14	315.17	53.50	0.0001	Significant
	Residual	88.37	15	5.89			
	Total	4500.76	29				

strate the role of process parametric variation on the response variables by using 3D surface plots (refer to Fig. 5, 6, and 7). Figure 5(a) reveals the trend of variation of MT as a function of the interaction between pulse on time and current.

Figure 5(a) reveals the trend of variation of MT as a function of the interaction between pulse on time and current. It is observed that the interplay between pulse on time and current is absent in causing any changes in MT, while MT appears to be affected solely by current as the slope of the surface changes only in the direction of the current. With the increase in current, the influx of heat on the work material's surface increases which ameliorates the rate of material erosion through liquefaction and vaporization of the work material. Such phenomena depict the situation when the current increases from 10 to 11 Ampere. However, MT increases marginally when the current increases from 11 to 12 Ampere, as in such situation debris may accumulate in the interelectrode gap due to vigorous melting and inadequate flushing, which promotes arcs and short circuits. The response surface in Fig. 5(b) demonstrates the trend of variation of MT driven by the interaction between pulse off time and current. MT is observed to attain the minimum as the current reaches 11 Ampere, and the pulse off time is maintained at its lowest value (40 μs). Such current and pulse off time setting is conducive to large heat accumulation in

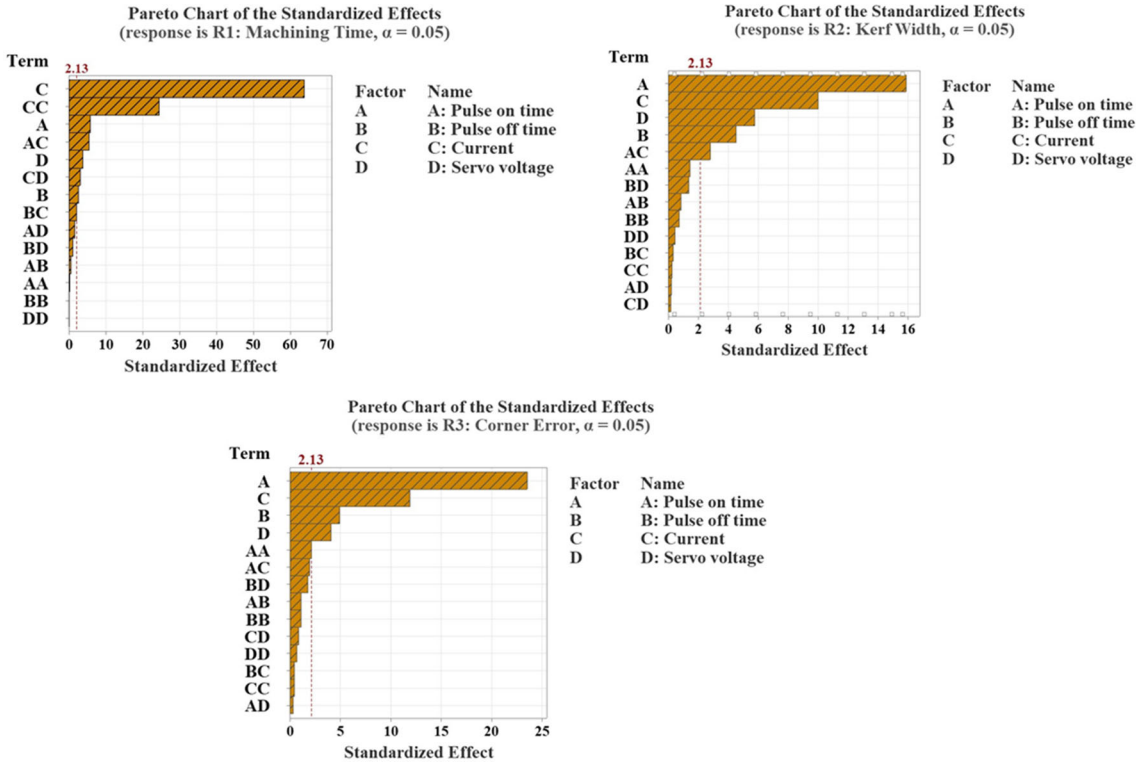

Fig. 3 Pareto chart analysis for the response variables (a) MT, (b) KW, (c) CE

the interelectrode gap due to the occurrence of a large number of high intensity sparks. However, at 12 Ampere current, even though the pulse off time is at its lowest, the machining time slightly increases due to debris piling up in the interelectrode gap as previously described. MT appears to be longer when the current is at its lowest and the pulse off time is at its highest. Under such situation, the content of heat accumulation in the interelectrode gap is low due to low intensity sparks and larger transmission of heat to the dielectric fluid. Machining time becomes minimum when the current is 11 Ampere, and the servo voltage is 30 V, which is evident from the response surface in Fig. 5(c). With a high current of 11 Ampere and a low servo voltage of 30 V, the spark generates high heat in the interelectrode gap with less dissipation of spark energy to the environment due to a narrower spark gap, retaining the spark's intensity and triggering severe melting and vaporization of the work material. In contrast, the machining time remains higher when the current is 10 Ampere, and the servo voltage is 50 V. With a minimum current, i.e., 10 Ampere, and a high value of servo voltage, i.e., 50 V, the spark causes less generation of heat in the interelectrode gap with more dissipation of spark energy to the environment due to wider interelectrode gap, thereby unable to restrain the intensity of the generated spark which undermines the melting and vaporization of the work material.

The response surface of kerf width resulting from the interaction between current and pulse on time is illustrated in Fig. 6(a). Kerf width attains the top position of the response surface (maximum) when both the interacting parameters (pulse on time and current) are at their maximum. Kumar et al. (Ref 33) documented similar observations in WEDM of Al-SiC-B_4C hybrid metal matrix composite. The maximum value of pulse on time and current leads to the existence of high temperature plasma channel in the spark gap for a longer duration promoting a large quantity of heat energy in the spark gap ensuing tremendous heat transfer on the workpiece surface which enables fusion and vaporization of a large chunk of material thereby forming large craters on the machined surface leading to maximum kerf width. The kerf width attains a minimum position on the response surface when both the interacting parameters, i.e., pulse on time and current, are minimum. The setting of minimum pulse on time and current possibly leads to the existence of low temperature plasma channel in the spark gap for a shorter duration fostering the small-scale generation of heat energy in the spark gap conducive to minimum heat transfer on the workpiece surface thereby leading to minimal melting and vaporization of the workpiece resulting in small-sized craters on the machined surface eventuating in minimum kerf width. As evident in Fig. 6(b), kerf width is the maximum when the current is maximum (12 Ampere) and the pulse off time is minimum (40 μs). With a maximum current of 12 Ampere and with the minimum pulse off time of 40 μs, there is a strong possibility of exorbitant heat energy transfer to the workpiece from the spark gap triggering the formation of large craters resulting in large kerf width on account of substantial melting and vaporization of the workpiece. This is possibly because of the maximum current that leads to maximum temperature of the plasma channel and minimum pulse off time undermines the flow of heat from the spark gap to the flowing dielectric fluid. The kerf width is minimum when the current is minimum (10 Ampere) and the pulse off time is maximum (50 μs), as can be noticed in Fig. 6(b). There is a small flow of heat energy to the work material from the spark gap with a current of 10 Ampere and pulse off time of 50 μs as minimum current of 10 Ampere induces low temperature in the plasma channel and maximum

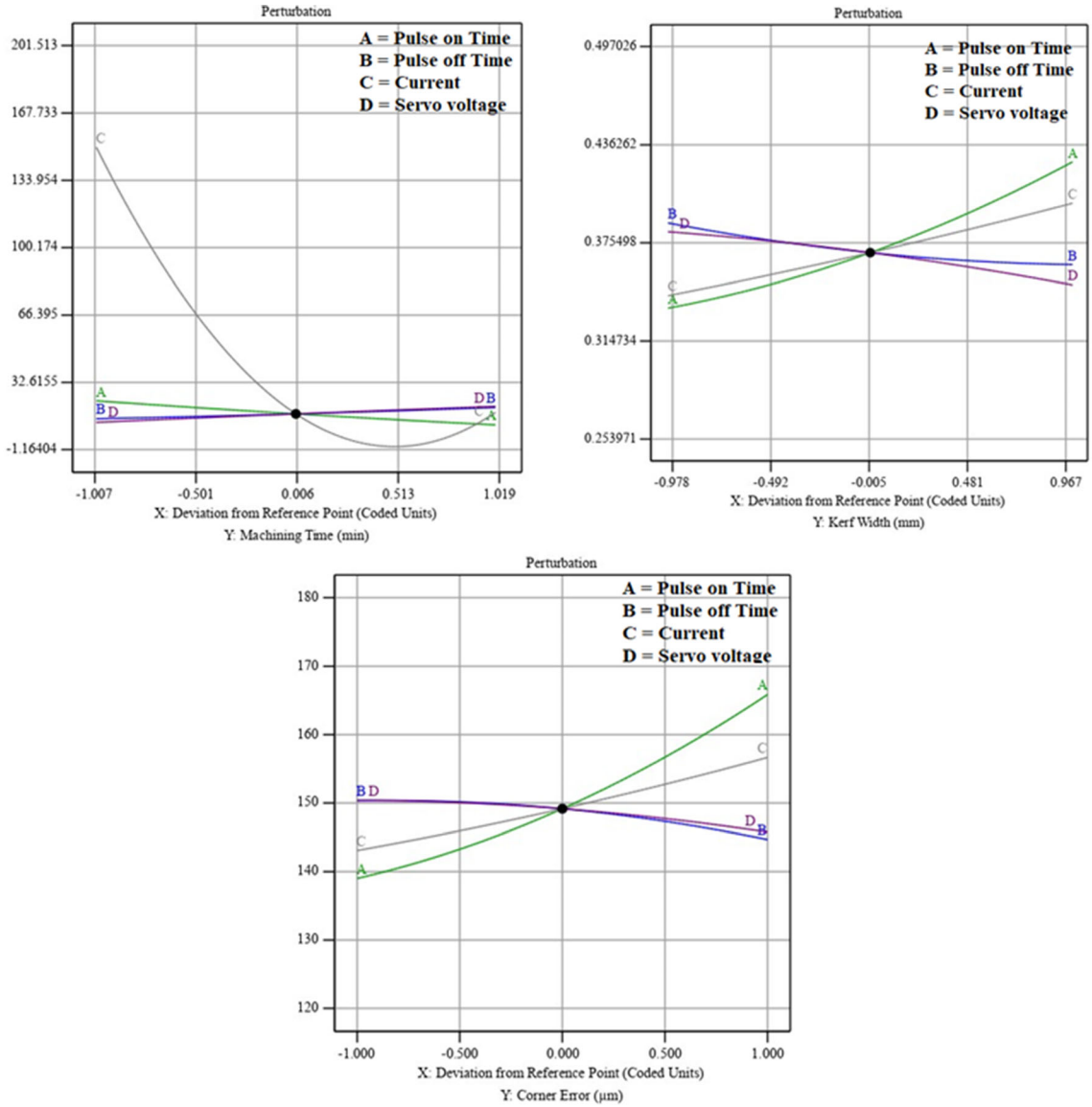

Fig. 4 (a) Perturbation plot for machining time, (b) Perturbation plot for kerf width, and (c) Perturbation plot for corner error

pulse off time of 50 μs promotes substantial flow of heat from the spark gap to the dielectric fluid. The combined effect of such parametric setting triggers meager melting and vaporization of the workpiece leading to the formation of small craters resulting in minimum kerf width. Figure 6(c) reveals the compound effect of current and servo voltage on the kerf width. It can be noticed that kerf width becomes maximum when the current is 12 Ampere and the servo voltage is 30 V. With maximum current, i.e., 12 Ampere, and a minimum servo voltage, i.e., 30 V, there is a possibility that the excessive heat energy that is developed in the interelectrode gap because of maximum current gets transmitted to the work material without significant loss to the dielectric fluid, as the interelectrode gap remains narrow with the minimum servo voltage. The kerf width is likely to become maximum due to formation of large craters due to vigorous melting and vaporization in such situation. However, when the current is 10 Ampere, and the servo voltage is 50 V, the kerf width is minimum due to the evolution of small craters due to inadequate melting and vaporization of work material. This is possibly because of the low heat generated by the spark in the interelectrode gap on account of minimum current and significant dissipation of heat energy to the dielectric fluid due to the wider interelectrode gap because of maximum servo voltage.

The response surface of corner error as a function of the interaction between pulse on time and current is illustrated in Fig. 7(a). It is evident that corner error is maximum at a maximum pulse on time of 128 μs and maximum current of 12 Ampere. This is due to the fact that the wire experiences large spark forces due to the high energized spark (as discharge

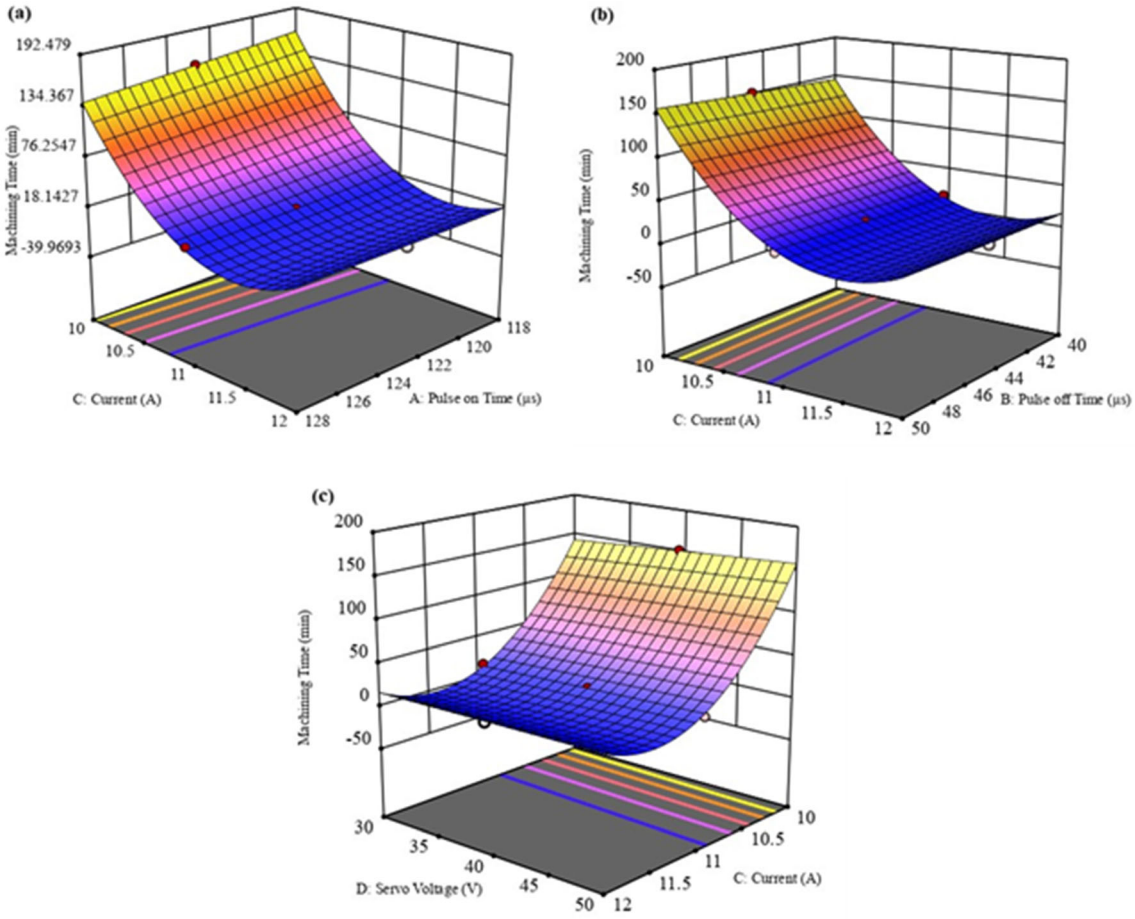

Fig. 5 (a) Response surface revealing the interplay between pulse on time and current on MT, (b) response surface revealing the interplay between pulse off time and current on MT, and (c) response surface revealing the interplay between servo voltage and current on MT

energy is proportional to pulse on time and current) and substantial bubble generation as a consequence of such setting, which results in huge wire lag and thereby maximum corner error. Whereas corner error minimizes at a minimum pulse on time of 118 μs and minimum current of 10 Ampere due to the negligible spark forces experienced by the wire owing to the low energized spark and negligible bubble concentration, which results in minimum wire lag and thereby minimum corner error. The aforesaid discussion is in parity with the findings reported by Bisaria et al. (Ref 34). Corner error becomes maximum if the current and pulse off time are tuned to their maximum and minimum value, respectively (refer to Fig. 7b). This is a consequence of large number of high intensified sparks that is experienced by the wire electrode, which causes adequate wire lag and thereby leading to maximum corner error. The corner error is minimum when the current is minimum and the pulse off time is the maximum as observed in Fig. 7(b). This is due to minimal number of low intensified sparks experienced by the wire at such setting resulting in less wire deflection and thereby minimum corner error. The variation of corner error as a function of the servo voltage and current is revealed in Fig. 7(c). Corner error is maximum as the current increases to maximum and the servo voltage is lowered to its minimum. With a maximum current of 12 Ampere and a minimum servo voltage of 30 V, the spark energy and the intensity of spark becomes maximum. The maximum energy of the spark is due to the maximum current and the intensity of spark becomes maximum due to the constriction of the spark gap on account of minimum servo voltage. Such situation leads to high spark forces on the wire resulting in large wire deflection and thereby large corner error. Conversely, if the current is set to its minimum value of 10 Ampere and the servo voltage is set to its maximum value of 50 V, the energy of the spark and the intensity of spark substantially falls owing to the minimum

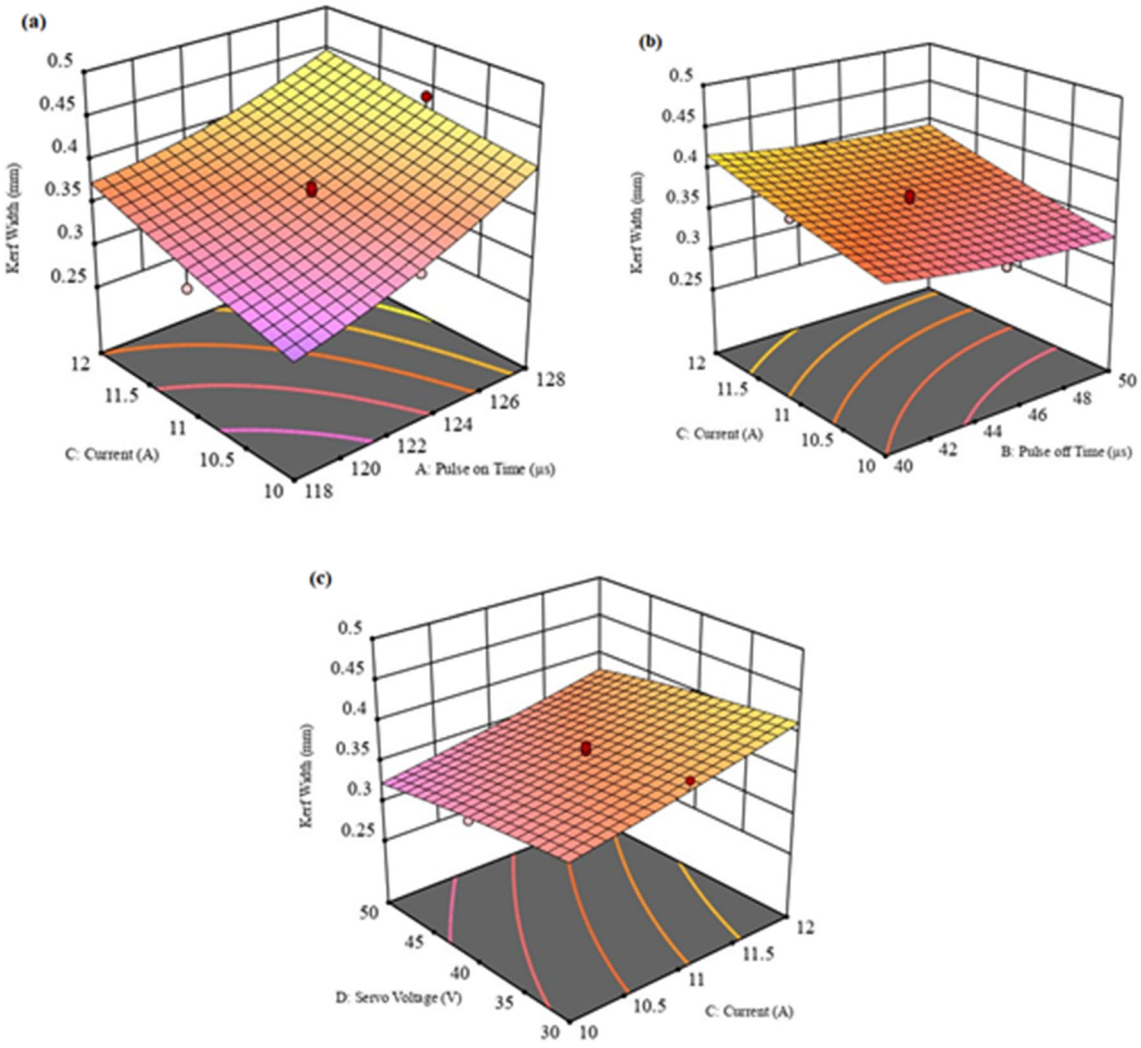

Fig. 6 (a) Response surface revealing the interplay between pulse on time and current on KW, (b) response surface revealing the interplay between pulse off time and current on KW, and (c) Response surface revealing the interplay between servo voltage and current on KW

value of current and the widening of the spark gap, respectively (Ref 35). This results in lower spark forces and thereby smaller corner error.

4. Surface Topography and Elemental Transformation Analysis

4.1 FESEM Analysis

The morphological structure of the machined surfaces is revealed by utilizing FESEM analysis for two samples in two different parametric settings. These settings such as (1) Pulse on time = 118 μs, Pulse off time = 50 μs, Current = 10 Ampere, Servo voltage = 50 V, and (2) Pulse on time = 128 μs, Pulse off time = 40 μs, Current = 12 Ampere, Servo voltage = 30 V are particularly conducive to low discharge energy, and high discharge energy, respectively. The FESEM micrograph for low discharge energy reveals shallow craters (refer to Fig. 8a). Because of the low discharge energy of the sparks, the thermal agitation due to the spark is inadequate to cause large material erosion from the work material resulting in shallow craters. On the other hand, the FESEM micrograph for high discharge energy exhibits deep craters (refer to Fig. 8b). This is due to large-scale material erosion from the work material due to large thermal agitation caused due to high discharge energy of the sparks. Low

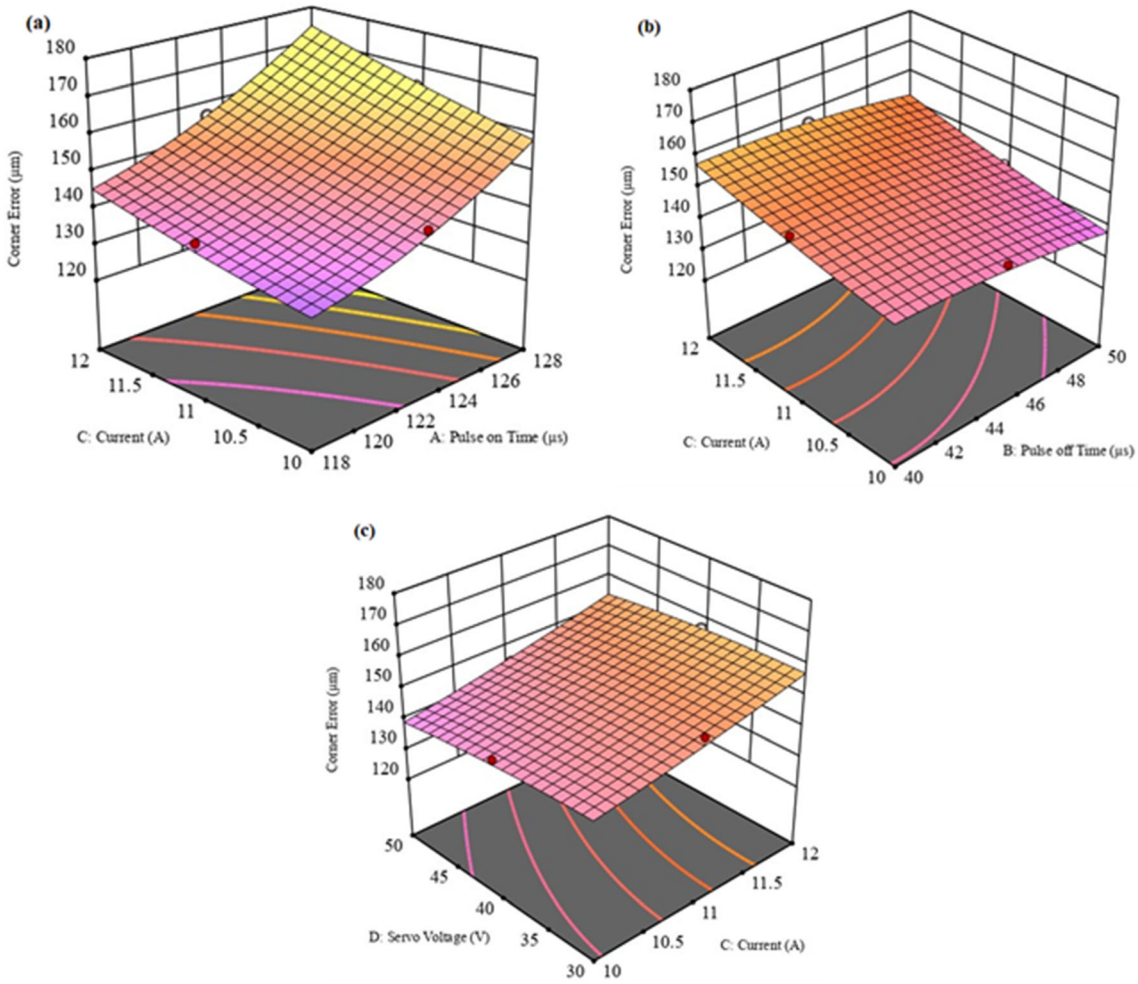

Fig. 7 (a) Response surface revealing the interplay between pulse on time and current on CE, (b) Response surface revealing the interplay between pulse off time and current on CE, and (c) Response surface revealing the interplay between of servo voltage and current on CE

discharge energy settings result in small melted deposits and fewer small voids, as can be noticed in Fig. 8(a). Conversely, Fig. 8(b) exhibits huge melted deposits and a significant number of large voids, which correlate to high discharge energy settings. Large-scale material melting occurs at high discharge energy levels, increasing the possibility of molten material re-solidification due to insufficient flushing, resulting in large-sized melted deposits. The likelihood of large-scale material vaporization is higher at high discharge energy settings which stimulates large-scale trapping of vapor bubbles on the re-solidified material, resulting in many big-sized voids. Microcracks appear on the machined surface for high discharge energy settings, whereas there is no evidence of such micro-cracks on the machined surface for low discharge energy settings. High discharge energy causes a large thermal gradient across the work material, inducing large thermal stresses which exceed the fracture strength of the work material, and results in microcracks.

4.2 Energy Dispersive X-ray Analysis

Energy dispersive x-ray analysis is employed to reveal the compositional changes encountered while WEDM machining of NAB alloy. The weight percentage of the constituent

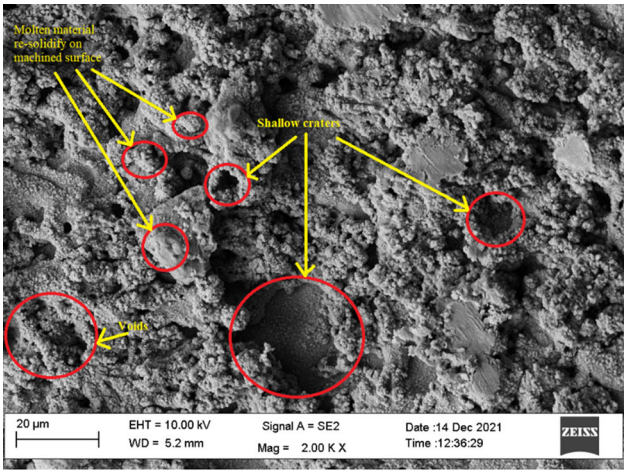

(a)

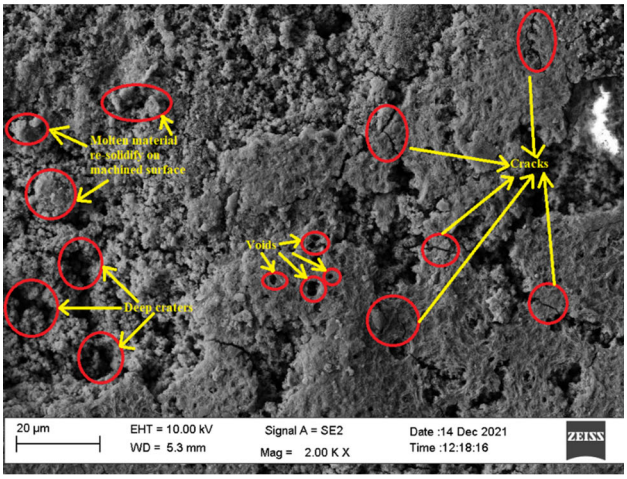

(b)

Fig. 8 (a) FESEM micrograph image of NAB alloy after WEDM at low discharge energy setting (Pulse on time = 118 μs, Pulse off time = 50 μs, Current = 10 Ampere, Servo voltage = 50 Volts), (b) FESEM micrograph image of NAB alloy after WEDM at high discharge energy setting (Pulse on time = 128 μs, Pulse off time = 40 μs, Current = 12 Ampere, Servo voltage = 30 Volts)

elements of the machined surface and unmachined surface is revealed in Table 4. The changes in weight percentage of zinc and copper are worth highlighting; the weight percentage of zinc has tremendously increased due to diffusion of zinc from the wire to the work material. However, the weight percentage of copper has slightly reduced due to the formation of intermetallic phase (refer to Table 4). EDX mapping of the marked region corroborates the formation of intermetallic phases (refer to Fig. 9). The weight percent of Fe, Ni, and Al of the machined surface as shown in Table 4 has diminished from the parent material due to formation of intermetallic phases. Whereas the percentage weight of manganese of the machined sample remains almost same as the parent material due to high melting point.

5. Conclusion

In the present work, we have undergone an experimental investigation to comprehend the domination of WEDM input features on machining time, kerf dimension, and corner error while machining complex profiles on NAB alloy through WEDM. RSM is exploited to mathematically model the response variables and analyze the effect of process parametric variation on the response variables. Following inferences are extracted from the current research:

1. Pareto chart for machining time (MT) reveals that current (*C*) is relatively the most influential process variable, followed by pulse on time (*A*), servo voltage (*D*), and pulse off time (*B*). Pareto chart for kerf width (KW) reveals that pulse on time (*A*) is relatively most influential process variable followed by current (*C*), servo voltage (*D*), and pulse off time (*B*). Pareto chart for corner error (CE) reveals that pulse on time (*A*) is relatively most influential process variable followed by current (*C*), pulse off time (*B*), and servo voltage (*D*).
2. FESEM images revealed the generation of a huge number of large-sized voids, large melted deposits, deep craters, and microcracks on the surface processed through WEDM at high discharge energy settings. Whereas due

Table 4 Chemical composition of the machined and unmachined sample

Element	Percentage weight of elements, wt.%(machined sample)	Percentage weight of elements, wt.%(unmachined sample)
Cu K	52.13	75.804
Zn K	25.16	0.32
Fe K	4.49	6
Ni K	2.23	4
Al K	15.23	13
Mn K	0.77	0.71

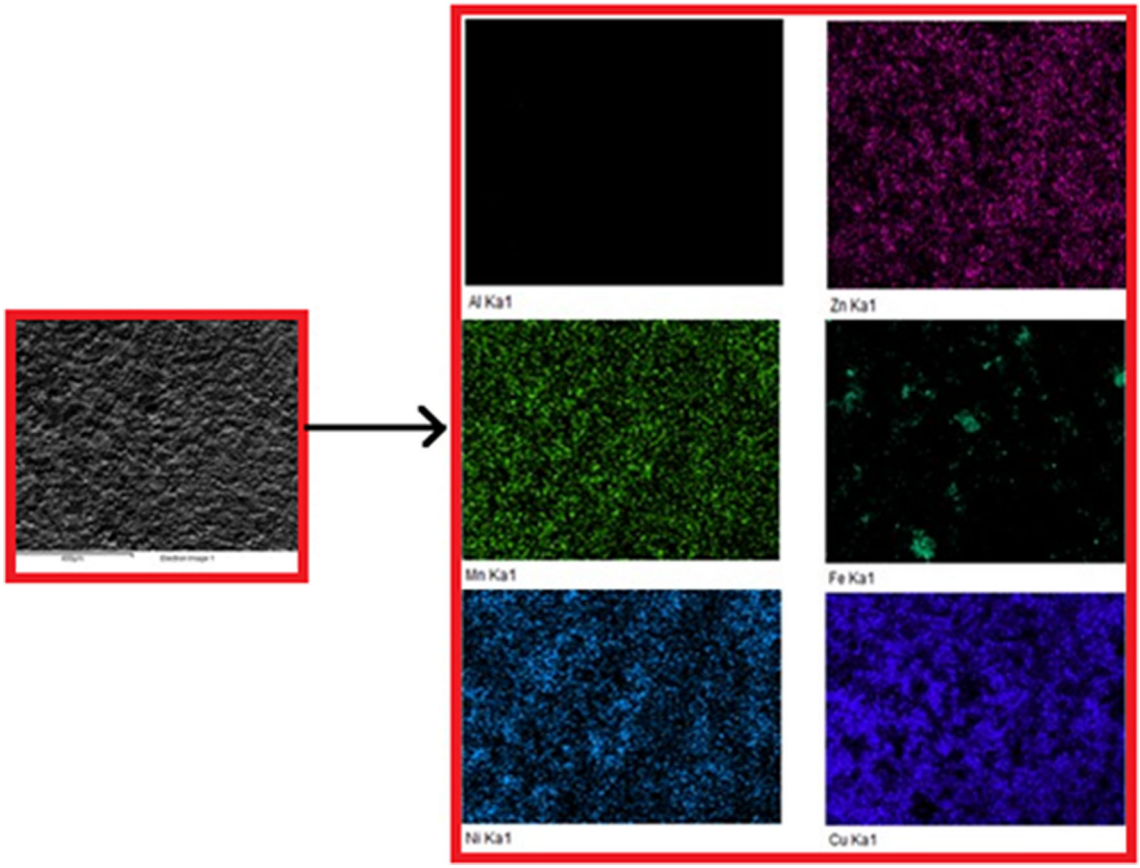

Fig. 9 EDX mapping of WEDM machined surface

to low energy spark, there are small-sized voids, small melted deposits, and shallow craters on the WEDM processed surface. The presence of microcrack is not evident on the surface processed through WEDM at low discharge energy level.

3. EDX analysis revealed that zinc has adequately deposited on the machined surface due to the large-scale diffusion from the zinc-coated brass wire.

Acknowledgment

DKS and SS are grateful for the financial support from MoE, India, during the research work.

Conflict of interest

The author(s) declared no potential conflicts of interest with respect to the research, authorship, and/or publication of the article.

References

1. K. Mouralova, J. Kovar, L. Klakurkova, J. Bednar, L. Benes and R. Zahradnicek, Analysis of Surface Morphology and Topography of Pure Aluminium Machined using WEDM, *Measurement*, 2018, **114**, p 169–176.
2. R.J. Ferrara and T.E. Caton, Review of Dealloying of Cast Aluminum Bronze and Nickel-Aluminum Bronze Alloys in Sea Water Service, *Mater Perform.*, 1982, **21**(2), p 30–34.
3. D.H.A. Al-Ethari, H. Hamza, Tool Life Modeling for Drilling NAB Alloy Reinforced by SIC and Graphite. Int. J. Eng. Innov. Technol. **3**(7) (2014)
4. Z.T. Fu, W.Y. Yang, S.Q. Zeng, B.P. Guo and S.B. Hu, Identification of Constitutive Model Parameters for Nickel Aluminum Bronze in Machining, *Trans. Nonferrous Met. Soc. China*, 2016, **26**(4), p 1105–1111.
5. R. Zhou and W. Yang, Analytical Modeling of Residual Stress in Helical End Milling of Nickel-Aluminum Bronze, *Int. J. Adv. Manuf. Technol.*, 2017, **89**(1), p 987–996.
6. G. Selvakumar, S. Sarkar and S. Mitra, An Experimental Analysis of Single Pass Cutting of Aluminium 5083 Alloy in Different Corner Angles through WEDM, *Int. J. Mach. Mach. Mater.*, 2013, **13**(2–3), p 262–275.
7. P. Lakshmanan, A. Arumugam, S. Palani and S. Kulothungan, Analyzing the Dimensional Deviation in Wire Cut Electric Discharge Machining of Nickel Aluminium Bronze using Molybdenum Wire Electrode, *Mater. Today Proc.*, 2021, **46**, p 1028–1032.
8. S. Saha, S.R. Maity, S. Dey and S. Dutta, Modeling and Combined Application of MOEA/D and TOPSIS to Optimize WEDM Performances of A286 Superalloy, *Soft Comput.*, 2021, **25**(23), p 14697–14713.
9. H. Majumder and K. Maity, Prediction and Optimization of Surface Roughness and Micro-hardness using grnn and MOORA-Fuzzy-a MCDM Approach for Nitinol in WEDM, *Measurement*, 2018, **118**, p 1–13.
10. H.R. Tonday and A.M. Tigga, An Empirical Evaluation and Optimization of Performance Parameters of Wire Electrical Discharge Machining in Cutting of Inconel 718, *Measurement*, 2019, **140**, p 185–196.
11. A. Kumar, N. Grover, A. Manna, R. Kumar, J.S. Chohan, S. Singh, S. Singh and C.I. Pruncu, Multi-objective Optimization of WEDM of Aluminum Hybrid Composites using AHP and Genetic Algorithm, *Arab. J. Sci. Eng.*, 2022, **47**(7), p 8031–8043.

12. P. Sharma, D. Chakradhar and S. Narendranath, Effect of Wire Material on Productivity and Surface Integrity of WEDM-Processed Inconel 706 for Aircraft Application, *J. Mater. Eng. Perform.*, 2016, **25**(9), p 3672–3681.
13. H. Bisaria and P. Shandilya, Experimental Investigation on Wire Electric Discharge Machining (WEDM) of Nimonic C-263 Superalloy, *Mater. Manuf. Process.*, 2019, **34**(1), p 83–92.
14. S. Saha, K.K. Gupta, S.R. Maity and S. Dey, Data-Driven Probabilistic Performance of Wire EDM: A Machine Learning Based Approach, *Proc. Inst. Mech. Eng. Part B J. Eng. Manuf.*, 2022, **236**(6–7), p 908–919.
15. F. Han, J. Jiang and D. Yu, Influence of Machining Parameters on Surface Roughness in Finish Cut of WEDM, *Int. J. Adv. Manuf. Technol.*, 2007, **34**(5), p 538–546.
16. M. Sadeghi, H. Razavi, A. Esmaeilzadeh and F. Kolahan, Optimization of Cutting Conditions in WEDM Process using Regression Modelling and Tabu-Search Algorithm, *Proc. Inst. Mech. Eng. Part B J. Eng. Manuf.*, 2011, **225**(10), p 1825–1834.
17. N. Sharma, R. Khanna, R.D. Gupta and R. Sharma, Modeling and Multiresponse Optimization on WEDM for HSLA by RSM, *Int. J. Adv. Manuf. Technol.*, 2013, **67**(9), p 2269–2281.
18. P.H. Yu, H.K. Lee, Y.X. Lin, S.J. Qin, B.H. Yan and F.Y. Huang, Machining Characteristics of Polycrystalline Silicon by Wire Electrical Discharge Machining, *Mater. Manuf. Process.*, 2011, **26**(12), p 1443–1450.
19. N.G. Patil and P.K. Brahmankar, Some Studies into Wire Electro-Discharge Machining of Alumina Particulate-Reinforced Aluminum Matrix Composites, *Int. J. Adv. Manuf. Technol.*, 2010, **48**(5), p 537–555.
20. S. Saha, S.R. Maity and S. Dey, Experimental Investigation of Dimensional Deviation of Square Punches Cut by Wire EDM of A286 superalloy, *Recent Advances in Mechanical Engineering*. Springer, Singapore, 2021, p 677–684
21. N. Sharma, T. Raj and K.K. Jangra, Parameter Optimization and Experimental Study on Wire Electrical Discharge Machining of Porous Ni40Ti60 Alloy, *Proc. Inst. Mech. Eng. Part B J. Eng. Manuf.*, 2017, **231**(6), p 956–970.
22. E. Beni, P. Lakshmanan and S.C. Amith, *Wire-Cut Electric Discharge Machining on Nickel-Aluminium-Bronze using Brass Wire Electrode. Trends in Manufacturing and Engineering Management*, Springer, 2021, p 67–74
23. P. Gupta, R. Khanna, R.D. Gupta and N. Sharma, Effect of Process Parameters on Kerf Width in WEDM for HSLA using Response Surface Methodology, *J. Eng. Technol.*, 2012, **2**(1), p 1–6.
24. W.L. Dekeyser, Geometrical Accuracy of Wire-EDM. The 9th International Symposium on EectroMachining, (1989), pp. 226–232
25. C.T. Lin, I.F. Chung and S.Y. Huang, Improvement of Machining Accuracy by Fuzzy Logic at Corner Parts for Wire-EDM, *Fuzzy Sets Syst.*, 2001, **122**(3), p 499–511.
26. G. Selvakumar, S. Sarkar and S. Mitra, Experimental Investigation on Die Corner Accuracy for Wire Electrical Discharge Machining of Monel 400 Alloy, *Proc. Inst. Mech. Eng. Part B J. Eng. Manuf.*, 2012, **226**(10), p 1694–1704.
27. G. Selvakumar, K. Bravilin Jiju, S. Sarkar and S. Mitra, Enhancing Die Corner Accuracy through Trim Cut in WEDM, *Int. J. Adv. Manuf. Technol.*, 2016, **83**(5), p 791–803.
28. H. Yan, K.D. Bakadiasa, Z. Chen, Z. Yan, H. Zhou and F. Han, Attainment of High Corner Accuracy for Thin-Walled Sharp-Corner Part by WEDM Based on Magnetic Field-Assisted Method and Parameter Optimization, *Int. J. Adv. Manuf. Technol.*, 2020, **106**(11), p 4845–4857.
29. K. Mandal, S. Sarkar, S. Mitra and D. Bose, Parametric Analysis and GRA Approach in WEDM of Al 7075 Alloy, *Mater. Today Proc.*, 2020, **26**, p 660–664.
30. H. Bisaria and P. Shandilya, Experimental Studies on Electrical Discharge Wire Cutting of Ni-Rich NiTi Shape Memory Alloy, *Mater. Manuf. Process.*, 2018, **33**(9), p 977–985.
31. H. Bisaria and P. Shandilya, Study on Effect of Machining Parameters on Performance Characteristics of Ni-Rich NiTi Shape Memory Alloy during Wire Electric Discharge Machining, *Mater. Today Proc.*, 2018, **5**(2), p 3316–3324.
32. S. Saha, S.R. Maity and S. Dey, Machinability Study of A286 Superalloy for Complex Profile Generation through Wire Electric Discharge Machining, *Arab. J. Sci. Eng.*, 2022 https://doi.org/10.1007/s13369-022-07028-5
33. S.S. Kumar, F. Erdemir, T. Varol, S.T. Kumaran, M. Uthayakumar and A. Canakci, Investigation of WEDM Process Parameters of Al-SiC-B4C Composites using Response Surface Methodology, *Int. J. Lightweight Mater. Manuf.*, 2020, **3**(2), p 127–135.
34. H. Bisaria and P. Shandilya, Processing of Curved Profiles on Ni-Rich Nickel-Titanium Shape Memory Alloy by WEDM, *Mater. Manuf. Process.*, 2019, **34**(12), p 1333–1341.
35. J.A. Sanchez, L.N. López de Lacalle and A. Lamikiz, A Computer-Aided System for the Optimization of the Accuracy of the Wire Electro-Discharge Machining Process, *Int. J. Comput. Integr. Manuf.*, 2004, **17**(5), p 413–420.